Environmental Science Nano

ROYAL SOCIETY OF CHEMISTRY

PAPER

View Article Online
View Journal

Cite this: DOI: 10.1039/d0en00953a

Emerging investigator series: 3D printed graphene-biopolymer aerogels for water contaminant removal: a proof of concept†

Arvid Masud,[a] Chi Zhou[b] and Nirupam Aich *[a]

Received 14th September 2020,
Accepted 3rd December 2020

DOI: 10.1039/d0en00953a

rsc.li/es-nano

Graphene-based 3D macroscopic aerogels with their hierarchical porous structures and mechanical strength have been widely explored for removing contaminants from water. However, their large-scale manufacturing and application in various water treatment processes are limited by their scalability. In this study, we report a proof-of-concept direct ink writing (DIW) 3D printing technique and subsequent freeze-drying to prepare graphene-biopolymer aerogels for water treatment. To provide appropriate rheology for DIW printability, two bio-inspired polymers, polydopamine (PDA) and bovine serum albumin (BSA), were added to the graphene-based ink. The biopolymers also contributed to the contaminant removal capacity of the resultant graphene-polydopamine-bovine serum albumin (G-PDA-BSA) aerogel. The physicochemical properties of the aerogel were thoroughly characterized from the nano- to macroscale. The 3D printed aerogel exhibited excellent water contaminant removal performance for heavy metals (Cr(VI), Pb(II)), organic dyes (cationic methylene blue and anionic Evans blue), and organic solvents (*n*-hexane, *n*-heptane, and toluene) in batch adsorption studies. The electrostatic interaction dominated the removal of heavy metals and dyes while the hydrophobic interaction dominated the removal of organic solvents from water. Moreover, the aerogel showed superb regeneration and reuse potential. The aerogel removed 100% organic solvents over 10 cycles of regeneration and reuse; additionally, the removal efficiencies for methylene blue decreased by 2–20% after the third cycle. The fit-for-design 3D printed aerogel was also effectively used as a bottle-cap flow-through filter for dye removal. The potential and vision of the 3D printing approach for graphene-based water treatment presented here can be extended to other functional nanomaterials, can enable shape-specific applications of fit-for-purpose adsorbents/reactors and point-of-use filters, and can materialize the large-scale manufacturing of nano-enabled water treatment devices and technologies.

Environmental significance

3D macroporous graphene aerogels emerged as promising nano-adsorbents with provisions for regeneration and reuse along with eliminating the risks of nanoparticle release during their application in water treatment. However, the aerogel synthesis process relies on the self-assembly of individual graphene nanosheets which remains a barrier against their large-scale manufacturing and applications. We presented here that we can utilize 3D printing to develop graphene-biopolymer aerogels that have hierarchical porous structures, present structural integrity in aqueous media, have promising removal performance for a wide-range of contaminants, and show excellent regeneration and reuse potential. Our approach of 3D printing graphene-based aerogels for contaminant removal can be extrapolated further to other nanomaterials to develop multifunctional nano-enabled adsorbents, filters, membranes, or reactors.

1. Introduction

Two-dimensional nanoscale carbon allotrope graphene and its derivatives *e.g.*, graphene oxide (GO) have emerged as promising adsorbents for diverse pollutants including textile dyes, heavy metals, and organic contaminants.[1] Their superior pollutant removal capability can be attributed to the high specific surface area,[2] ease of surface functionalization,[3] and ability to exert simultaneous electrostatic, hydrophobic, and/or pi–pi interactions.[4,5] However, one of the major barriers that exists for GO's large scale application as a nano-adsorbent is in its high colloidal stability in water making recovery of GO nanosheets from water treatment processes quite difficult. To alleviate such issues, three-dimensional (3D) macroscopic structures known as aerogels made from self-assembled 2D GO

[a] *Department of Civil, Structural and Environmental Engineering, University at Buffalo, The State University of New York, Buffalo, NY 14260, USA. E-mail: nirupama@buffalo.edu*
[b] *Department of Industrial and Systems Engineering, University at Buffalo, The State University of New York, Buffalo, NY 14260, USA*

† Electronic supplementary information (ESI) available. See DOI: 10.1039/d0en00953a

nanosheets have recently emerged as promising nano-adsorbents. These graphene-based 3D macrostructures with tunable porosity, geometry, and surface chemistry provide interconnected pores for high mass transport and high adsorption capacity for diverse contaminants, are ultralight, offer the provisions to be regenerated and recycled, and eliminate the risks of nanoparticle release.[6]

Nevertheless, the large-scale manufacturing and deployment of macroscopic graphene aerogels in water treatment are limited due to processing challenges. One major reason behind this is the lack of precise control over the bulk 3D design that is a prerequisite for fit-for-design aerogels to be incorporated into geometrically optimized reactors, columns, and filters for contaminant removal from water.[7] Conventional synthesis routes for graphene hydrogels/aerogels include batch processing through hydrothermal[8,9] or solvothermal[3] reduction, *in situ* chemical reduction,[10] direct cross-linking,[11] and template guided (*e.g.*, metallic foam[12]) deposition and freeze casting.[13] These processes rely majorly on the *in situ* self-assembly or gelation of precursor GO suspension and cannot offer precise control over the macroscopic architecture of the synthesized graphene monoliths.[14] The architectural flexibility and scalability of template guided deposition[12] and freeze casting[13] methods are also compromised due to their template mediated process. Therefore, conventional graphene aerogel synthesis processes lack the scalability for continuous industrial level manufacturing and also lack the control over their size, shape and architecture.

3D printing or additive manufacturing has emerged as an enabling technology for the continuous fabrication of highly complex physical structures from computer-aided design through bottom-up synthesis processes. Particularly, direct ink writing (DIW), a robust, low-cost and scalable 3D printing technique, employs continuous and robotic extrusion of layer-by-layer ink material to fabricate a pre-designed 3D product by regulating the motion of the micro-extruder and the printing stage in three axes.[15,16] The unique ability of 3D printing to provide scalability, flexibility of architectures, and design-mediated functionality is introduced for applications in water and wastewater treatment processes *e.g.*, membranes and filters,[17] biological growth media,[18] and chemical and photocatalytic-reactors.[19] Few recent reports also proposed nanoscale adsorbents such as metal–organic frameworks[20] and nanoscale carbon nitride (C_3N_4)[21] for water contaminant removal. DIW 3D printing has been recently used to fabricate graphene-based aerogel structure for different applications, including supercapacitors,[22–24] batteries,[16] biomedical[25] and thermal devices.[26] These studies showed the ability of 3D printing to fabricate graphene-based aerogels with controllable macro-architecture up to sub-millimeter precision yet with hierarchical porous structures, which cannot be achieved by conventional self-assembly processes. Even with such promising advantages, no studies have presented the applicability of 3D printed graphene-based aerogels for water treatment. The major challenge remains in the preparation of a graphene-based ink that has both the appropriate viscoelasticity and shear-thinning properties required for achieving effective DIW 3D printing. Many times, to achieve this, ultra-high concentration (≥80 mg mL^{-1}) of graphene ink is used[16,26] – which can cause agglomeration and inhomogeneity within the graphene network, and thus, compromise the inherent graphene properties.[23] Furthermore, printed graphene-based aerogels need to hold their structural integrity in aqueous media and perform water contaminant adsorption.

In this study, we aimed to alleviate these above challenges of 3D printability and water stability of graphene-based aerogels and to demonstrate a proof-of-concept process for DIW 3D printing of a graphene-biopolymer aerogel that can be used in water treatment applications. We hypothesized that graphene surface modification using selected biopolymeric additives can enable 3D printability, water stability, and contaminant removal ability of graphene-based aerogels. For this, we chose two bio-inspired polymers, polydopamine (PDA) and bovine serum albumin (BSA), as viscosifying additives for achieving the appropriate viscoelastic rheology for DIW 3D printing of graphene aerogels. Furthermore, these polymers are well known for modifying GO surfaces for adsorption of diverse contaminants *e.g.*, heavy metals,[27,28] dyes,[29,30] and organic contaminants.[31,32] We synthesized a viscoelasticity-optimized ink from graphene-polydopamine-bovine serum albumin (G-PDA-BSA) dispersion, 3D printed a self-standing cylindrical structure with submillimeter precision, and subsequently freeze-dried to obtain the G-PDA-BSA aerogel. We characterized the hierarchical porous structure and physicochemical properties of 3D printed aerogels using nanoscale X-ray computed tomography (nano-CT), Brunauer–Emmett–Teller (BET) surface area, pycnometer, scanning and high-resolution transmission electron microscopy (SEM and HRTEM), electron dispersive X-ray spectroscopy (EDS), X-ray diffraction (XRD), Raman and Fourier transform infrared (FTIR) spectroscopy, thermogravimetric analysis (TGA), and zeta potential measurement. The G-PDA-BSA aerogels were tested for the batch adsorption of a wide-range of water contaminants to show the potential application of these 3D printed aerogels as nano-adsorbents for water treatment. These contaminants include cationic and anionic dyes *i.e.*, methylene blue (MB) and Evans blue (EB), respectively, heavy metals *i.e.*, chromium (Cr(VI)) and lead (Pb(II)), and organic solvents *i.e.*, *n*-hexane, *n*-heptane, and toluene. Finally, the applicability of 3D printed fit-for-design G-PDA-BSA aerogels for water filtration was tested for MB removal using a 3D printed bottle-cap flow-through filtration system.

2. Materials and methods

2.1 Materials

Single-layer graphene oxide (GO) (>99.3 wt%, thickness 0.43–1.23 nm) (US Research Nanomaterials, Inc., Houston, TX), dopamine hydrochloride (Sigma-Aldrich, St. Louis, MO), and

lyophilized bovine serum albumin (BSA, Fisher Scientific, Fair Lawn, NJ) were used as purchased. TRIS (tris(hydroxymethyl aminomethane)) buffered saline, lead nitrate ($PbNO_3$, ≥99%), and Evans blue (EB or $C_{34}H_{24}N_6Na_4O_{14}S_4$) were purchased from Sigma-Aldrich (St. Louis, MO). Methylene blue (MB or $C_{16}H_{18}ClN_3S$, Fisher Scientific, Fair Lawn, NJ), potassium dichromate ($K_2Cr_2O_7$, 99.99%, Mallinckrodt Baker, Inc., Phillipsburg, NJ), *n*-hexane (C_6H_{14}, ≥99%, Acros Organics, Geel, Belgium), *n*-heptane (C_7H_{16}, ≥99%, Acros Organics, Geel, Belgium) and toluene (C_7H_8, 99%, Fisher Scientific, Fair Lawn, NJ) were also used as purchased.

2.2 G-PDA-BSA ink preparation and characterization

GO nanosheets at a concentration of 30 mg mL^{-1} were dispersed in 20 mM Tris buffered solution by sonicating for 2 hours (8 s pulse on followed by 2 s pulse off, amplitude 50, input power 15–18 watts) with a microtip (1/16″) based ultrasonic dismembrator (Q 700, Qsonica Sonicators, Newtown, CT). Then, dry dopamine hydrochloride powder (15 mg mL^{-1}) was added to the dispersion and sonicated for 10 minutes at the same pulse on–off period and sonication power. The pH of the dispersion was adjusted to 8.5 with ammonium hydroxide (NH_4OH). The dispersion was then heated at 60 °C for 6 hours under magnetic stirring at 300 rpm on a hot plate stirrer for self-polymerization of polydopamine (PDA) to occur, which resulted in G-PDA dispersion. The dispersion was left to rest at room temperature for 24 hours. Then 1.5 mL of a 300 mg mL^{-1} aqueous dispersion of BSA was mixed with 5 mL of the above-prepared G-PDA dispersion using a bath sonicator (Branson, 2800, Danbury, CT). This G-PDA-BSA dispersion was thermally cured at 85 °C in an oven for 1 hour to induce the BSA mediated gelation, which formed a viscoelastic G-PDA-BSA ink. The apparent viscosities of the 3D printing ink during the fabrication process were measured with a rotational viscometer (NDJ-5S, M&A Instruments Inc., China) at different shear rates.

2.3 Method of 3D printing and freeze-drying

Fig. S1† presents a flow-chart that shows different steps of the ink preparation and 3D printing process. A retrofitted Ultimaker 2 GO (brand name; not graphene oxide) fused deposition modelling (FDM) 3D printer (Ultimaker B.V., MA) was used as the host framework for printing the aerogel. A 10 mL syringe barrel connected with a 600 μm diameter micro-nozzle was mounted on a holder that can move along the *XY* direction following the designed toolpath generated by the printing software. The G-PDA-BSA ink was placed in the syringe barrel and was extruded through the nozzle by controlling the air pressure through a dispenser (Performus X100, Nordson Corporation, East Providence, RI). The base with a removable metallic substrate plate moved down one layer at a time in the *Z* direction after each layer of printing was completed. A CAD model of a cylindrical structure with a diameter of 12 mm and height of 4 mm was converted into printing instructions using a computer program (Slic3r). The 3D printer followed the programmed instructions to print a cylindrical structure with G-PDA-BSA ink, replicable to the CAD model. The printing was executed using a printing speed of 20 mm s^{-1} and an individual layer height of 500 μm. The printed cylindrical G-PDA-BSA gel was transferred to a freezer (temperature −18 °C) to initiate ice crystallization. The frozen gel was then freeze-dried (Labconco FreeZone Triad, Kansas City, MO) for 24 hours to obtain the final G-PDA-BSA aerogel. These aerogels were kept at 85 °C for 2 hours in an oven to remove any excess water.

2.4 Characterization of 3D printed aerogels

The macroporous structure of the 3D printed G-PDA-BSA aerogel was characterized with nanoscale X-ray computed tomography (nano-CT, Zeiss Versa 520, White Plains, NY) in the Biotechnology Resource Center Imaging Facility (BRC) at Cornell University. The X-ray source was operated with an accelerating voltage of 60 KV. A 20× objective was used at a final resolution of 380 nm per pixel. For preventing any disturbance to the aerogel structure, the whole sample was mounted inside the instrument. A total of 1930 unbinned fluoroscopy images were captured with an exposure time of 10 seconds per image. The reconstructed 3D images were cropped to a volume of 1845 × 1845 × 700 voxels (700 × 700 × 266 μm). Further data processing for manual thresholding and volume rendering was performed with Avizo™ (ThermoFisher Scientific™) software. The skeletal volume and density of the aerogel were calculated with a pycnometer (Micromeritics Accu-Pyc II 1340, Norcross, GA) using pressurized helium gas. The porosity (Π) of the aerogel was calculated from this skeletal density and bulk density measured from physical dimensions of the aerogels obtained with a vernier caliper.

The micro- and nano-structural architecture and morphology of the G-PDA-BSA aerogels and GO nanosheets were analyzed using focused ion beam scanning electron microscopy (FIB-SEM, Carl Zeiss AURIGA, White Plains, NY) and high-resolution transmission electron microscopy (HRTEM, JEOL JEM 2010, JEOL USA, Inc., Peabody, MA). For SEM characterization of the aerogel, a thin section of the aerogel was cut from the middle of the monolith using a sharp razor and was placed on a stub using double-sided adhesive carbon tape. An SPI-Module™ (West Chester, PA) was used to deposit a thin layer of gold to make the sample conductive for SEM imaging. HRTEM was carried out with an accelerating voltage of 200 KV. HRTEM samples were prepared by ultrasonicating 1 mg of the aerogel in 10 mL ethanol for 10 min. Then, 1 mL of this suspension was placed on a carbon-coated copper grid (100 mesh, Ted Pella, Inc.) and dried before analysis. The elemental composition of the samples was analyzed with a field emission scanning electron microscope (Hitachi SU70, Japan) coupled with an Oxford energy dispersive spectrometer (EDS, Oxford Instruments, Concord, MA). A Micromeritics Tri-Star II instrument (Micromeritics, Norcross, GA) was used to obtain

the N_2 adsorption–desorption isotherms of the GO nanosheets and G-PDA-BSA aerogels. The isotherm data were used to calculate the specific surface area and pore size distribution (PSD) based on the Brunauer–Emmett–Teller (BET) theory and non-local density functional theory (NLDFT) slit pore model, respectively.[33]

The crystallographic fingerprint of the aerogels was identified with X-ray diffraction (XRD, Rigaku Ultima IV, Rigaku Corporation, Wilmington, MA) using a scan rate of 2° min^{-1} and step size of 0.02°. Information on molecular vibration and defects in crystallographic structures of the samples were analyzed using Raman spectroscopy (Renishaw InVia, Renishaw plc., West Dundee, IL) with an incident excitation wavelength of 514 nm. Fourier-transform infrared (FTIR) spectroscopy (1760 FTIR, Perkin-Elmer, Waltham, MA) was performed to analyze the composition and covalent bonding of functional groups present in the sample. The thermal response and stability of the samples in air was characterized using thermogravimetric analysis (TGA, Micromeritics Instrument Corp., Norcross, GA) with a ramp rate of 10 °C min^{-1} up to 1000 °C. The surface charge of the aerogels was determined from measuring the zeta potential of aerogel powders in aqueous media using a Malvern Zetasizer Nano-ZS particle analyzer (Westborough, MA).

2.5 Water contaminant removal by 3D printed aerogels

Batch adsorption experiments were performed with the 3D printed G-PDA-BSA aerogels to determine their water contaminant removal capacity for Cr(VI), Pb(II), MB, and EB at room temperature. In a typical experiment setup, cylindrical G-PDA-BSA aerogels, each with a mass of ~40 mg, were placed individually in separate glass vials containing 15 mL aqueous solution of individual contaminants at different initial concentrations. The vials were kept shaking in a rotary shaker for 96 hours at 150 rpm to reach adsorption equilibrium. In order to test the release of BSA from the aerogel, a similar experiment was carried out in DI water. After adsorption, the intact and free-standing aerogels were removed from the water and the final concentration of the contaminant was recorded. Cr(VI) concentrations were measured by spectrophotometric analysis using a 96-well plate with UV-vis spectrometry (SpectraMax® i3, San Jose, CA) using a chelating agent 1,5-diphenylcarbazide by comparing the optical response with a calibration curve as reported in our previous study.[34] Pb(II) concentrations were measured using an inductively coupled plasma optical emission spectrometer (ICP-OES) (iCAP 6000, Thermo Scientific, Grand Island, NY).[34] For determining MB, EB, and BSA concentrations, UV-vis spectrometric analysis (Cary 60, Agilent Technologies, Santa Clara, CA) was performed using a 3 mL cuvette at a wavelength of 665, 620, and 280 nm respectively.

For testing the removal of organic solvents *n*-hexane, *n*-heptane and toluene using the 3D printed aerogel, a 300 μL solvent layer was placed over 3 mL of water in a measuring cylinder. The aerogels were placed on top of the solvent layer to remove the solvent from the solvent–water interphase. *n*-Hexane, *n*-heptane, and toluene removal capacity was calculated by measuring the weight of the aerogel before and after the removal experiments.

2.6 Regeneration and reuse of 3D printed aerogels

We tested the regeneration and reuse of 3D printed G-PDA-BSA aerogels for the removal of dye MB and organic solvents. In the case of MB, the free-standing aerogel, after reaching the adsorption equilibrium, was taken out of the vial and shaken in 15 mL ethanol (pH 2) in another glass vial at 150 rpm for 24 hours to allow desorption. After desorption, the aerogel was taken out and placed again in a vial with MB solution of desired concentration. This recycling process was repeated three times. For organic solvents, after solvent adsorption, the aerogels were taken out and heated for 20 minutes at 70 °C for *n*-hexane, 100 °C for *n*-heptane, and 115 °C for toluene to allow the evaporation of adsorbed solvents. Once the adsorbed solvents evaporated, the aerogels were again used for solvent removal as mentioned earlier. These regeneration and reuse cycles for the aerogels with organic solvents were repeated 10 times.

2.7 Flow-through filtration study with the 3D printed aerogel

A flow-through filtration study was performed with the 3D printed G-PDA-BSA aerogel using a bottle-cap filtration system. A perforated bottle-cap filter was designed with Fusion 360 (Autodesk Inc.) software and 3D printed with a FDM 3D printer with polylactic acid (PLA) filament. This filter system was designed to hold and fit the 3D printed G-PDA-BSA aerogel adsorbent for contaminated water to pass through it. The G-PDA-BSA aerogel was 3D printed with cylindrical dimensions of 14 mm diameter and 14 mm height to fit into the bottle-cap filter system. An aqueous solution of 1 ppm MB was passed through the filtration system with a hydrostatic pressure of 736 Pa under gravity. The MB concentration of the effluent was measured at different intervals to evaluate the MB removal performance of the filtration system.

3. Results and discussion

3.1 Viscoelasticity and printability of the G-PDA-BSA ink

For preparing a graphene-based ink that is usable in a DIW 3D printing process, two biopolymers PDA and BSA were incorporated. Fig. 1a shows the steps of the G-PDA-BSA ink synthesis process. The Tris buffer solution is known to enhance the dispersibility of GO by converting the epoxy groups on the basal planes of GO into hydroxyl groups through ring opening reaction.[35,36]

The addition of dopamine hydrochloride in the GO dispersion in Tris buffer at alkaline pH (pH = 8.5) enables the self-polymerization of PDA and subsequent PDA coating of the graphene surface. Hydrogen bonding and π–π interaction between these GO nanosheets, and affinity

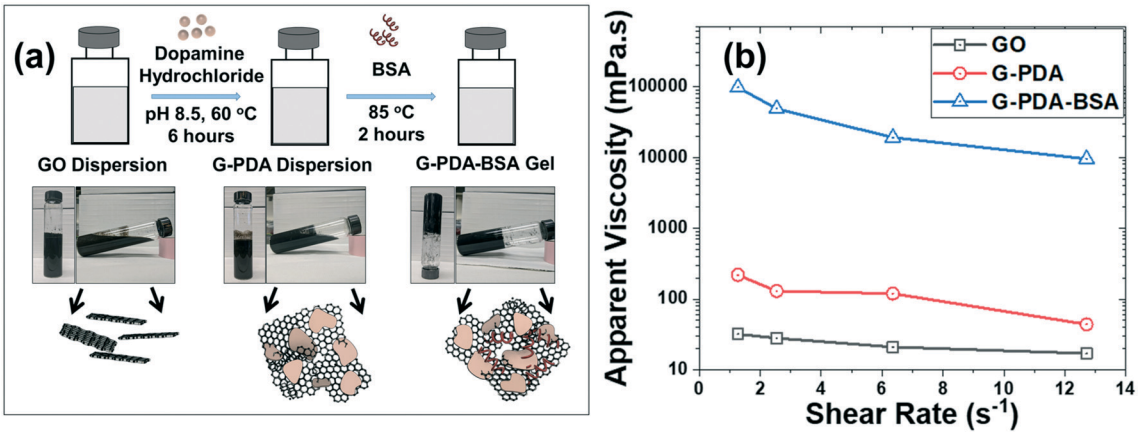

Fig. 1 (a) Schematic of different steps for the synthesis of the G-PDA-BSA viscous gel and (b) plot of apparent viscosity as a function of shear rate for GO, G-PDA, and G-PDA-BSA dispersions.

between PDA and graphene aromatic rings caused overlapping and coalescence of G-PDA layers.[37,38] This resulted in 1 order of magnitude increase in the apparent viscosity of the G-PDA ink from the GO ink, as shown in Fig. 1b and Table S1.† However, the G-PDA dispersion didn't attain the required viscoelasticity for DIW printability, as the G-PDA dispersion started flowing within the container when tilted because of gravity (Fig. 1a).

After the addition of BSA to the G-PDA dispersion, the oxidized catechol groups of PDA interacted with the thiol and amine groups of BSA through Michael addition or Schiff base reactions, resulting in a G-PDA-BSA dispersion.[39] When this G-PDA-BSA dispersion was heated (85 °C) beyond the transition temperature of BSA, heat-induced partial denaturation of BSA resulted in a decrease in the α-helix content and a subsequent increase in the β-sheet content.[40] Hydrogen bonding between the ordered β-sheets along with electrostatic interaction triggered gelation entrapping the solvent within the dispersion matrix.[40–42] The resulting viscous G-PDA-BSA gel could hold its shape against gravity, even when the container was placed upside down (Fig. 1a). The apparent viscosity of the G-PDA-BSA gel (98 300 mPa s) was almost 2 and 3 orders of magnitude higher than that of G-PDA (220 mPa s) and GO dispersion (32 mPa s), respectively, at a shear rate of 1.27 s^{-1} (Fig. 1b).[39] Also, a gradual decrease in apparent viscosity (from 98 300 to 9520 mPa s) with the increase in shear rate (from ~1 to ~12 s^{-1}) indicated that the G-PDA-BSA gel achieved adequate shear thinning properties and hence, its flowability under stress.[43] Thus, the G-PDA-BSA gel attained the required viscoelasticity and shear thinning properties of the DIW printable ink. Notably, to obtain this 3D printable ink, the ratio of GO, PDA, and BSA used was 1 : 0.5 : 3 which was optimized by performing trial and error experiments to achieve the above-mentioned required viscosity and shear thinning properties. The ratios for the trial and error experiments were selected based on previously reported GO : PDA and GO : BSA ratios in the literature that was used for graphene functionalization for water treatment.[29,44]

3.2 Porous structure and physical morphology of 3D printed G-PDA-BSA aerogels

The prepared G-PDA-BSA ink was directly printed as a free-standing structure based on a cylindrical CAD model that is shown in Fig. 2a. Fig. 2b shows the layer-by-layer DIW 3D printing process of the G-PDA-BSA hydrogel on the metal base. The printed hydrogels were further freeze-dried to attain ultra-light and free-standing G-PDA-BSA aerogels as shown on the top of a Kimwipe in Fig. 2c. The continuous and scalable 3D printing process produced replicable G-PDA-BSA aerogels as shown in Fig. 2d and e. Each of these aerogels had an individual mass of ~40 mg with a density of ~88 mg cm^{-3}.

Nanoscale X-ray computed tomography (nano-CT) was carried out to study the 3D interconnected macro-porous network within the undisturbed and monolithic G-PDA-BSA aerogel. Fig. 3a shows as obtained the high resolution (with a voxel side length of 380 nm) 3D reconstruction of the 3D printed aerogel through volume rendering with nano-CT data and presents the slightly contrasting graphitic matrix within the aerogel volume. Fig. 3b and Movie S1 (in the ESI†) present the noise-filtered version of the 3D reconstruction to clearly show the lamellar and bonded G-PDA-BSA material network in blue and also the void volumes (non-blue regions) confirming the connectivity among the macro-pores within the aerogel.

Videos showing the comprehensive 3D reconstructed 360° rotating views of the macroporous aerogel and segmented section (Fig. S2) are provided in ESI† Movies S1 and S2. The black rectangles in Fig. 3c represent the three axes along which images of 2D cross-sectional planes were obtained and are shown in Fig. 3(d–f). These images also confirm the connectivity of porous networks by showing the macroscopic void volumes (black regions) separated by the thin and densely packed lamellar G-PDA-BSA matrix (blue lines). The freeze-drying process during the aerogel synthesis first transformed the water trapped within the G-PDA-BSA hydrogel to ice crystals. The volume expansion of the ice

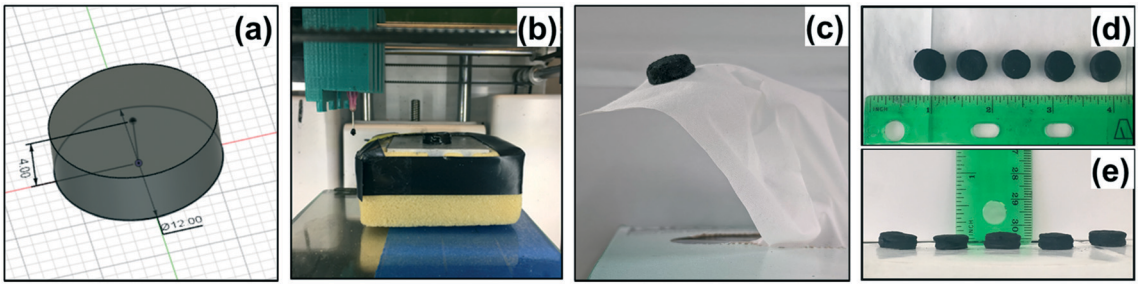

Fig. 2 (a) Cylindrical 3D CAD model, (b) DIW printed G-PDA-BSA hydrogel, (c) freeze dried ultra-light G-PDA-BSA aerogel on top of a Kim wipe, (d and e) top and front views of printed aerogels.

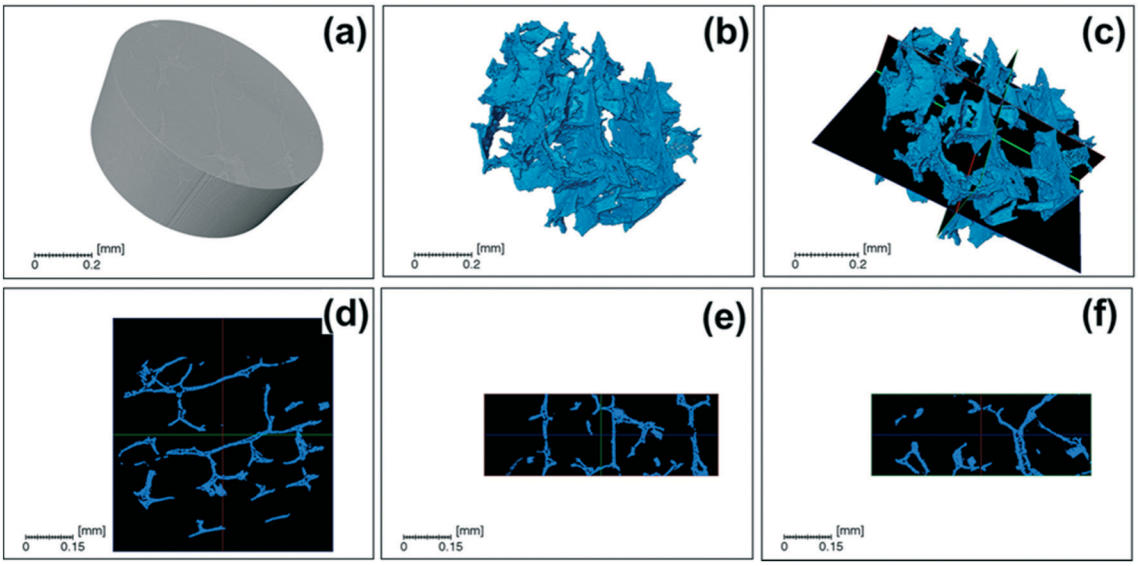

Fig. 3 3D volume rendering of nano-CT images (a) as-obtained and (b) noise filtered, and (d–f) representative cross-sectional nano-CT images along the direction shown in (c).

crystals creates pressure against the G-PDA-BSA graphene nanosheets to form the coalesced lamellar structures, and subsequent evaporation of the ice crystals creates interconnected macroscopic voids between these lamellar structures. The porous (void) volume fraction of the aerogel was calculated to be 89.1% from the voxel count of the nano-CT rendered volume, which was consistent with the value of 90.3% derived from the helium gas displacement pycnometer. These interconnected porous channels can promote the passage of liquid (or contaminated water) facilitating the interaction of contaminants with adsorbent materials throughout the monolithic structure.

SEM imaging was performed to study the morphology within the macro-pore walls or lamellar material network of 3D printed aerogel, since nano-CT cannot provide information about the sub-micron porous structure. Fig. 4(a–c) present the SEM images of the precursor GO while Fig. 4(d–f) present the similarly magnified images of the G-PDA-BSA aerogels. SEM images suggest relatively smoother planar sheets for GO with numerous layers aggregated on top of each other, whereas biopolymer functionalized graphene sheets (*i.e.*, G-PDA-BSA) were twisted and coalesced with each other in the case of the G-PDA-BSA aerogel to impart a porous structure. Pores with a wide size range (sub-micron to ~10 μm) were identified within the lamellar material network, however, these pores were much smaller compared to the continuous macro-porous channels (shown by nano-CT in the previous section) within the monolithic aerogel structure. This confirms that the 3D printed aerogel had a hierarchical porous structure. The dense packing and bonding of the graphene nanosheets within the lamellar material network of the aerogel can impart excellent mechanical strength,[45] which may have contributed to their excellent structural integrity during their application for contaminant removal from aqueous media.

The BET surface area calculated from the N_2 adsorption isotherm for the G-PDA-BSA aerogel was 9.86 $m^2\ g^{-1}$, which was more than double that of precursor GO (4.10 $m^2\ g^{-1}$) (Fig. S3a†). These low surface areas can be attributed to aggregation in the dry state,[46,47] and also functionalization of graphene surfaces.[48,49] The NLDFT pore size distribution indicates the presence of mesopores (<100 nm) in the G-

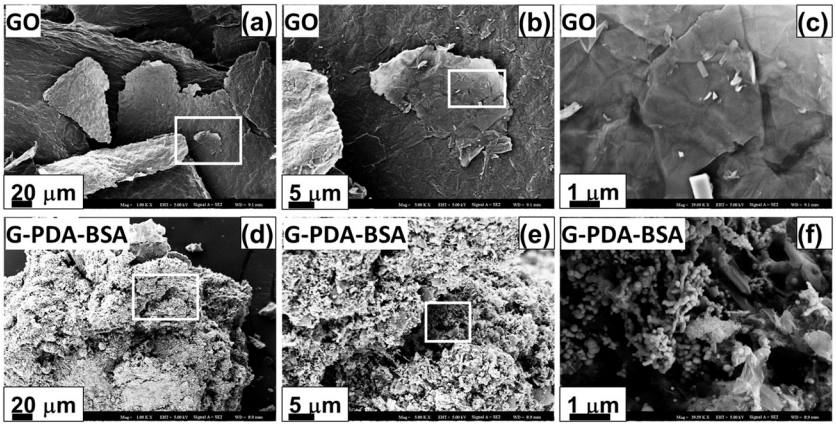

Fig. 4 SEM micrographs of (a–c) GO and (d–f) G-PDA-BSA aerogel at different magnifications. White rectangular boxes show the selected area which is magnified in the next (right) image.

PDA-BSA aerogel (Fig. S3c†). The differential mesopore volume for the G-PDA-BSA aerogel was 1 order of magnitude higher than that of precursor GO. These enhanced surface areas and mesopore volumes of the 3D printed aerogels can contribute significantly towards pollutant removal.

To comprehend the morphology of aerogel materials at the nanoscale, TEM images of the G-PDA-BSA aerogel were obtained and compared with those of GO. Fig. 5(a and b) present TEM images of GO showing their characteristic aggregated and few-layered 2D planar sheets. TEM images of G-PDA-BSA aerogels shown in Fig. 5(c and d) also show similar uniform 2D morphology, however, with wrinkled and folded regions of darker contrasts. Although PDA and BSA biopolymer layers are difficult to detect in TEM images,[39] the alteration in transparency suggests successful coating of graphene sheets by PDA and BSA layers. Some protuberances dispersed throughout the 2D layers can be attributed to the excess particulate formation of PDA or BSA clusters.

3.3 Chemical composition, defects, and crystallinity of the 3D printed aerogel

Fig. S4† presents the SEM images showing the selected regions of GO nanosheets and G-PDA-BSA aerogels and their corresponding EDS spectra for elemental composition. The nitrogen/carbon mass ratio increased from 0.03 for GO to 0.12 for G-PDA-BSA, while the oxygen/carbon ratio decreased from 0.47 to 0.20, respectively. These changes in the elemental composition can be attributed to the presence of amine-containing functional groups in the biopolymers and the reduction of oxygen functional groups of GO[50,51] that resulted in partially reduced GO (or rGO) in the G-PDA-BSA aerogel. The oxidative polymerization of PDA releases electrons which can also partially reduce GO.[38] Furthermore, BSA also reduces GO with tyrosine residues to restore the graphitic structure.[37,52]

Fig. 6a presents the XRD spectra of GO and G-PDA-BSA. While the XRD spectrum of GO contains a sharp diffraction peak at 2θ = 10.9° attributed to the oxidized graphitic sheets,[53] this diffraction peak is diminished in the case of the G-PDA-BSA aerogel. However, a characteristic peak from BSA at ~9.8° exists for the G-PDA-BSA aerogel.[54] The new broadened peak around 2θ = 23° in the spectra of the G-PDA-BSA aerogel can be attributed to cumulative contributions from graphitic carbon domains from BSA, reduced graphene oxide (rGO), and PDA.[54–56] Overlapping of XRD peaks from reduced graphene oxide and PDA around 2θ = 25°, and BSA around 2θ = 21° cause the peak to be flatter in this region for the aerogel.[54,57] This further confirms the reduction of GO in the aerogel and replacement of oxygen functional groups by the PDA and BSA polymer.

Broader and slightly right-shifted signal contribution from BSA (at 2θ = 9.8° and 2θ = 21°) in the aerogel – compared to the reported signals of pristine BSA (at 2θ = 9° and 2θ =

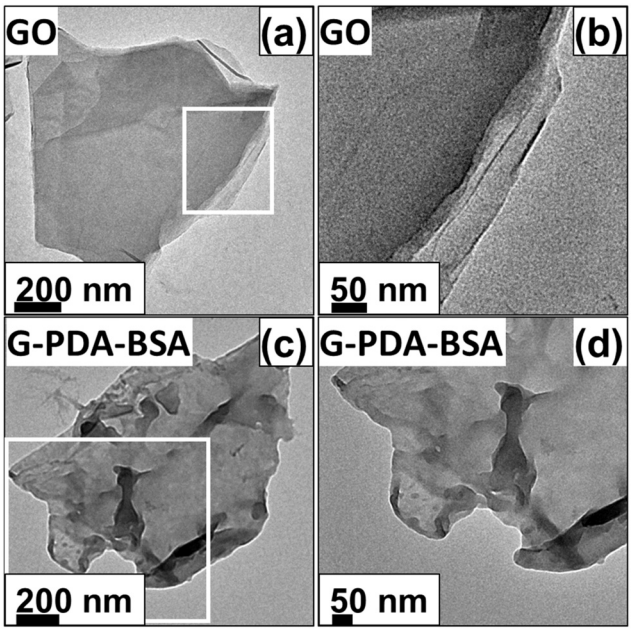

Fig. 5 TEM images of (a and b) GO nanosheets and (c and d) G-PDA-BSA aerogels at different magnifications. The right images are the magnified images of the white rectangular boxes in the left images.

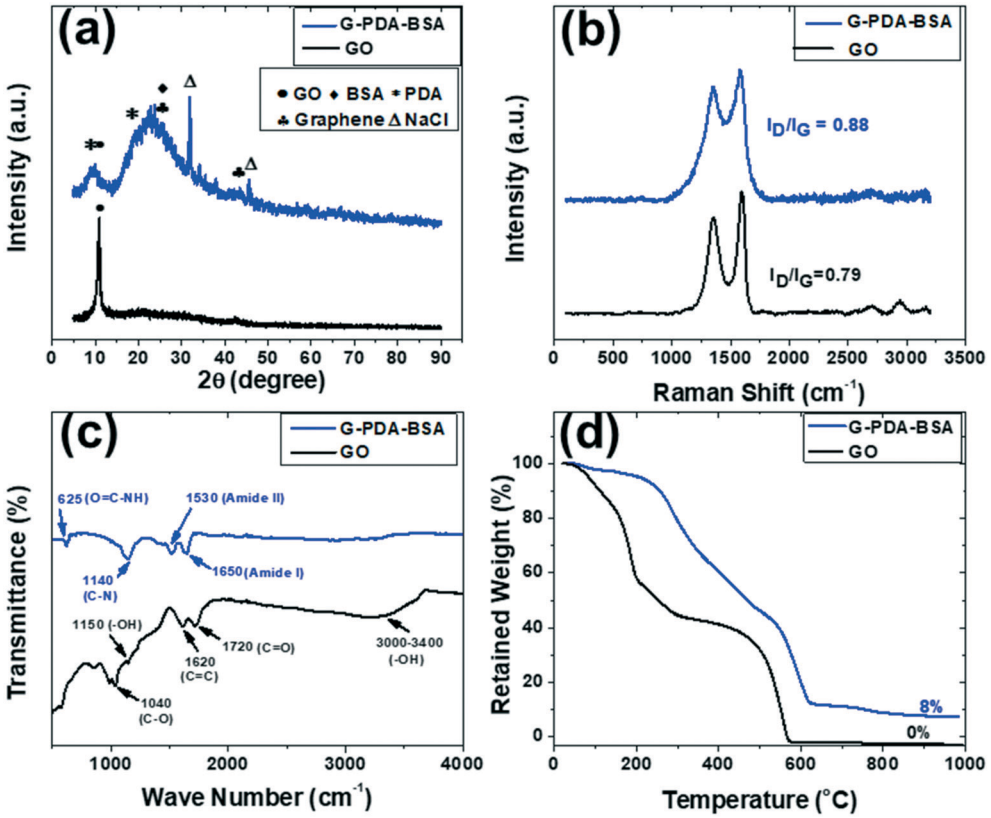

Fig. 6 (a) XRD, (b) Raman, and (c) FTIR spectra, and (d) TGA curves of GO nanosheets and G-PDA-BSA aerogels.

19.5°) can be attributed to denaturation of crystalline BSA while adsorbed on the surface of G-PDA.[54] The peaks at 2θ = 32° and 2θ = 45.5° occur due to residual NaCl that is present in Tris buffer saline.[58]

Fig. 6b presents the Raman spectra of GO and G-PDA-BSA. Both spectra show the two major peaks at 1600 cm^{-1} and 1350 cm^{-1} representative of the graphitic domain (G-peak) and defects (D-peak), respectively, in the G-PDA-BSA aerogel. The I_D/I_G ratio, which is a measure of disorder in the graphitic structure, increased from 0.79 for GO to 0.88 for the G-PDA-BSA aerogel. Such increase in the I_D/I_G ratio in the aerogel can be attributed to sp^3 hybridization of graphene sheets and bonding with amine functional groups from PDA and BSA,[59] hence, resulting in a more defective structure in the aerogel.

Fig. 6c presents the FTIR spectra of GO nanosheets and G-PDA-BSA aerogels. In the case of GO spectrum, peaks can be observed at 1040 cm^{-1} (C–O–C stretching vibration), 1150 cm^{-1} (–OH stretching vibration), 1720 cm^{-1} (OH–C═O vibration), and 3000–3400 cm^{-1} (phenolic hydroxyl groups), confirming the presence of different oxygen functional groups.[27,60] In the case of the G-PDA-BSA aerogel spectrum, the peaks at 1720 cm^{-1} and 3000–3400 cm^{-1} corresponding respectively to the vibration of –COOH and phenolic hydroxyl groups disappeared.[55,60] The peaks corresponding to other oxygen functional groups associated with GO also exhibited relatively lower intensity in the case of the aerogel. All of these confirm the reduction of GO in the G-PDA-BSA aerogel. There are new peaks at 1530 and 1650 cm^{-1} for the aerogel, which can be attributed to –NH– stretching of amide I and amide II.[39,61,62] Specifically, the peak at 1650 cm^{-1} can be attributed to the reaction between the carboxyl groups of GO and amine groups of PDA and BSA.[63] The broad nature of the peak can be attributed to the hydrogen-bonded β-sheets (as presented with a peak around 1620 cm^{-1}) formed due to denaturation during gelation of BSA.[40,64] The in-plane vibration at 630 cm^{-1} corresponding to O═C–NH also confirms the chemical bonding between GO and BSA.[27]

Fig. 6d presents the results of thermogravimetric analysis (TGA) which explains the thermal stability of the tested material. From the TGA curve of GO, the weight loss below 250 °C can be attributed to the decomposition of oxygen functional groups.[65] The relatively better thermal stability for G-PDA-BSA below 250 °C suggests the absence of oxygen functional groups, thus, reduction of GO in the aerogel and also bonding between lamellar graphene sheets through amine groups.[66] From 450–550 °C, there is a sharp and total weight loss for GO denoting aggressive thermal oxidation of graphitic carbon.[65] However, for G-PDA-BSA, the weight loss is gradual from 200–600 °C due to the presence of amorphous carbon from PDA and BSA.[67,68] The residual mass of 8% for the aerogel is due to the char residue formed from PDA and BSA.[67,68]

3.4 Contaminant removal by the 3D printed aerogel

The 3D printed G-PDA-BSA aerogel was tested for the removal of a wide array of aqueous contaminants including heavy metals, cationic and anionic dyes, and organic solvents. The monolithic aerogel was intact at the end of these removal tests, confirming its excellent mechanical strength and structural stability in aqueous solution. Moreover, the absence of BSA leached from the aerogel was also confirmed since no detectable concentration of BSA was found in DI water after soaking the G-PDA-BSA aerogel for 72 hours. Unfolding of hydrophobic sequences in BSA and subsequent gelation during the denaturation process can be attributed to the resistance against leaching of BSA.[69] Such structural integrity of the G-PDA-BSA aerogels during use in contaminant removal processes along with excellent aqueous stability is promising and showed the feasibility of using them in water treatment applications.

3.4.1 Heavy metal and dye removal by 3D printed aerogels. Fig. 7 presents the removal performances of G-PDA-BSA aerogels for batch adsorption of heavy metals and organic dyes tested in the range of their initial concentrations up to 200 ppm in water. The tested heavy metals include chromium (Cr(VI), Fig. 7a) and lead (Pb(II), Fig. 7b), and the tested dyes include cationic methylene blue (MB, Fig. 7c) and anionic Evans blue (EB, Fig. 7d). For heavy metals, the G-PDA-BSA aerogels showed the highest Cr(VI) and Pb(II) removal capacities of 45.05 and 43.76 mg g^{-1}, respectively, at their initial concentration of 200 ppm and unregulated pH of 4.3 and ~5.3, respectively. As minimum heavy metal concentration is often desired in treated drinking water, the removal percentage is also an important parameter in addition to the removal capacity. The G-PDA-BSA aerogels showed the highest 93% and 94% removal of Cr(VI) and Pb(II) ions, respectively, at an initial concentration of 25 ppm. For organic dyes, the highest removal capacity for MB and EB were 35.33 and 38.73 mg g^{-1}, respectively, when the pH of the adsorbate was unregulated at 3.9 and 4.3, respectively, at their initial concentration of 200 ppm. The removal efficiencies for MB and EB, on the other hand, were 99.17% and 87.30%, respectively, at their initial concentration of 25 ppm, suggesting better removal percentages of MB than EB at a lower concentration.

Fig. S5† presents the equilibrium adsorption isotherms for all four heavy metals and dyes, *i.e.*, Cr(VI), Pb(II), MB, and EB by the G-PDA-BSA aerogel that were fitted with the Langmuir and Freundlich adsorption isotherm model. The model parameters and adjusted R^2 values are summarized in Tables S2 and S3.† The equilibrium adsorption isotherms for all the contaminants were in better agreement with the Langmuir model (adjusted R^2 value 0.79–0.99) compared to the Freundlich model (adjusted R^2 value 0.65–0.96). This

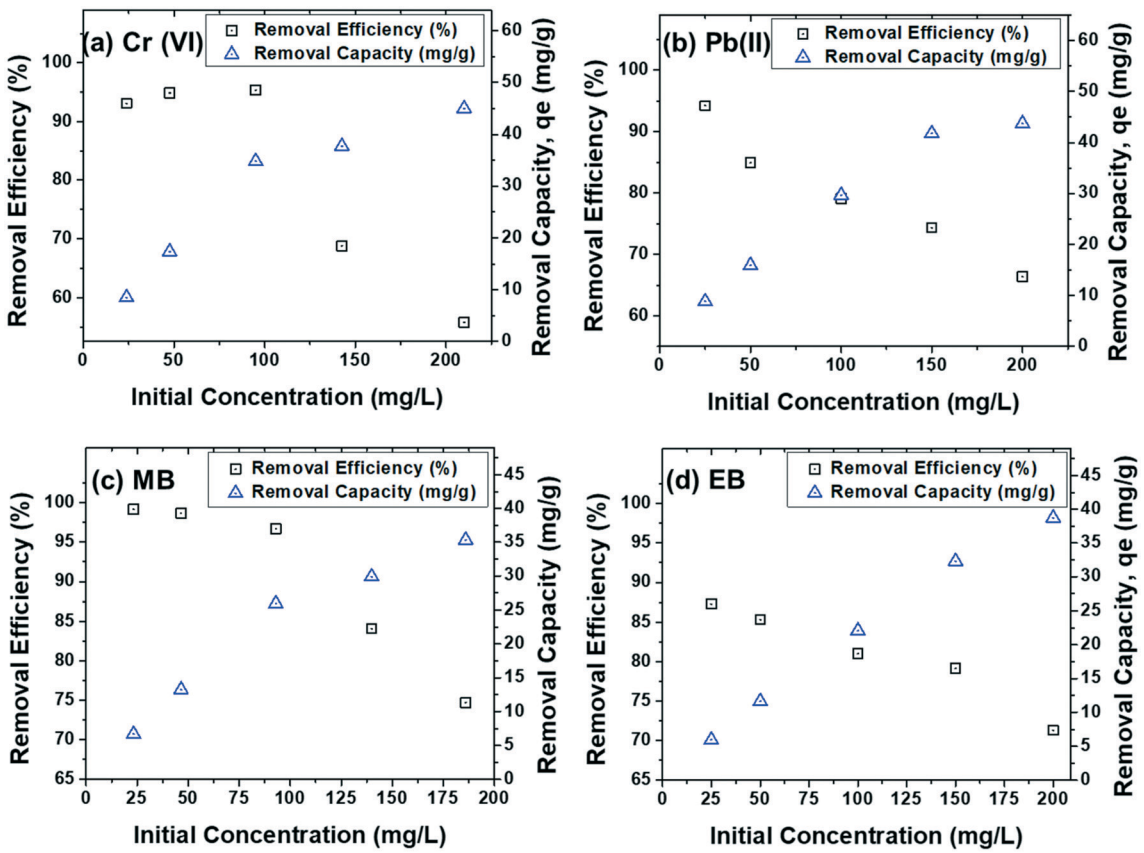

Fig. 7 (a) Cr(VI), (b) Pb(II), (c) MB and (d) EB removal performances of G-PDA-BSA aerogels at various initial concentrations of the contaminants. The pH remained unadjusted for these tests.

suggests monolayer adsorption of these contaminants on the G-PDA-BSA aerogel.[70,71]

3.4.2 Effect of pH on the contaminant removal by 3D printed aerogels. Fig. 8 presents the effect of pH on heavy metal and dye removal performance of the G-PDA-BSA aerogel for a pH range of 2–8 at the same initial concentration of 200 ppm. The pH range was kept below 8, as higher pH can cause hydrolysis and subsequent precipitation of heavy metal ions to form metal hydroxide before being removed by the aerogel.[72,73] Between the heavy metals, the removal capacity of the G-PDA-BSA aerogel for Pb(II) increased almost linearly from 18 mg g^{-1} at pH = 2 to 44.95 mg g^{-1} at pH = 6.5 and then started to plateau. However, for Cr(VI), the removal capacity slightly increased from 43.56 mg g^{-1} at pH = 2 to 47.23 mg g^{-1} at pH = 3.5 and then decreased very slowly but linearly reaching a value of 35.08 mg g^{-1} at pH = 8. Compared to the Pb(II) removal capacity which changed significantly with the pH change, the Cr(VI) removal capacity remained stable within the pH range.

In the case of dyes, similar to Pb(II), the removal capacity of cationic MB increased almost linearly from 30.75 mg g^{-1} at pH = 2 to 51.53 mg g^{-1} at pH = 8. However, for anionic EB, a slight decrease in the removal capacity was observed between acidic and alkaline pH. The removal capacities for EB were 39.36 mg g^{-1} at pH = 2 and 33.81 mg g^{-1} at pH = 8.

3.4.3 Mechanisms of interactions between contaminants and 3D printed aerogels. To elucidate the mechanisms of interactions between the contaminants and 3D printed aerogels, surface charge *i.e.*, the zeta potential values of GO nanosheets and G-PDA-BSA aerogels, was determined over a pH range of 2.5–10 and plotted as shown in Fig. 9a. The surface of G-PDA-BSA aerogels was more positively charged than the precursor GO nanosheets. This can be attributed to the presence of the amine functional groups of PDA and BSA in the aerogel.[74] The zeta potential of the G-PDA-BSA aerogels decreased with the increase of pH due to deprotonation of functional groups present in GO and in biopolymers and an isoelectric point was reached at pH = 5.7.[75,76] This suggests that at pH higher than 5.7, the G-PDA-BSA aerogel facilitated electrostatic attractions for the positively charged contaminants (at those pH) and subsequently resulted in their higher removal than in lower pH.[37] This was further confirmed with Pb(II) and MB removal, as the more negatively charged surface of the aerogel at higher pH facilitated greater removal of positively charged Pb^{2+} and MB ions with the increase of pH.[77] Some Pb(II) removal observed even at very low pH can be attributed to the complex formation with catechol or amino acid residues of PDA and BSA, respectively.[77–79]

For MB, hydrophobic interaction with the G-PDA-BSA aerogel contributed to its removal at low pH.[80] However, at pH < 8, the dominant aqueous species of Cr(VI) (*e.g.*, $HCrO_4^-$, $Cr_2O_7^{2-}$) and EB are negatively charged.[81] As a result, the Cr(VI) and EB removal does not increase with the increase of pH because of the interaction with the negatively charged G-PDA-BSA aerogel at increasing pH. However, the overall high Cr(VI) removal by the aerogel throughout the pH range can be attributed to protein–chromium complex formation as a removal mechanism.[82,83] For EB, in addition to protein-mediated complexation,[84] π–π interaction with the G-PDA-BSA aerogel through a large number of aromatic rings also contributed to the high removal capacity for EB across the pH range.[85]

3.4.4 Comparison between the removal performance of GO powder and 3D printed aerogels. The performance of the 3D printed G-PDA-BSA aerogel could not be compared with that of a control 3D printed graphene aerogel because without the presence of PDA and BSA, GO dispersions were not printable. Hence, we compared the contaminant removal performance of the G-PDA-BSA aerogel with that of GO nanosheets in powder form. The per gram cost of GO, PDA and BSA are ~195, 7, and 13 dollars, respectively.[86–88] Considering the higher cost of GO, approximately 15–25 times compared to PDA and BSA, the performance of G-PDA-BSA and GO powders was normalized with GO content for comparison. When normalized by GO content, the contaminant removal capacity of G-PDA-BSA aerogels was greater compared to that of GO for chromium (~3.7 times),

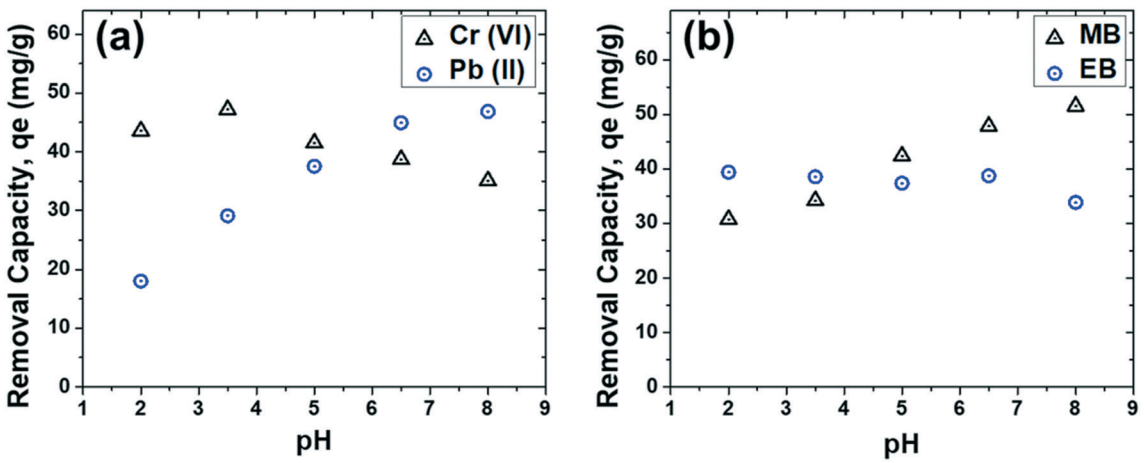

Fig. 8 The removal capacities for (a) Cr(VI) and Pb(II) and (b) MB and EB by the G-PDA-BSA aerogel at different pH values and at an initial concentration of 200 ppm.

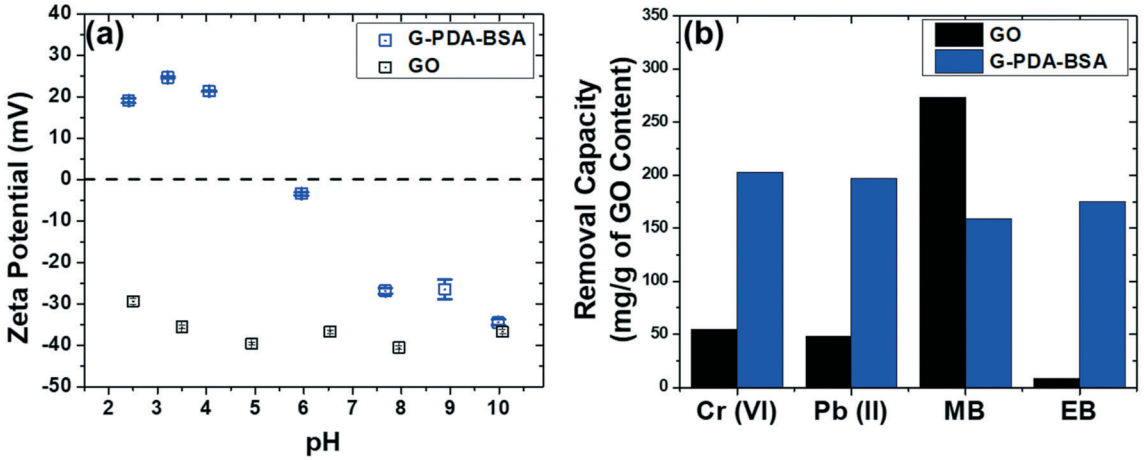

Fig. 9 (a) The zeta potential values of GO nanosheets and G-PDA-BSA aerogels in aqueous media at different pH values. (b) The removal capacity of GO powder and G-PDA-BSA aerogels normalized by their GO content for Cr(VI), Pb(II), MB, and EB. For all the contaminants, initial concentration = 200 mg L^{-1}, adsorbent dose = 10 mg, volume of adsorbate = 15 mL.

lead (~4.1 times), and EB (~20.2 times) – suggesting the merit of using PDA and BSA as additives for removing contaminants (Fig. 9b). However, the removal capacity of G-PDA-BSA aerogels for MB decreased by one-third compared to that of GO. As mentioned above, the positive surface charge of the G-PDA-BSA aerogel in pH lower than 5.7 causes electrostatic repulsion for the cationic MB and results in a lower adsorption capacity. However, GO is known to be negatively charged at any pH (Fig. 9a) and causes electrostatic attractions for MB which results in higher adsorption of MB by GO than that by G-PDA-BSA.

3.4.5 Recycling performance of 3D printed aerogels. The regeneration and reuse potential of the 3D printed G-PDA-BSA aerogels was tested by performing the separations of organic solvents and dyes from water. The tested organic solvents included *n*-hexane, *n*-heptane, and toluene while MB was used as the model dye. *n*-Hexane and *n*-heptane are constituents of gasoline that are obtained from refining crude oil. Toluene is a by-product of gasoline production. The aerogels were tested for the removal of *n*-hexane, *n*-heptane and toluene from the water interface. 300 μL of the organic solvents were added to water individually. Complete removal of all the organic solvents was achieved instantaneously (within ~5 seconds).

A total of 10 adsorption–desorption cycles were performed for testing the regeneration and reuse ability of the aerogel for these organic solvents which yield their complete removal every time as shown in Fig. 10(a). The hydrophobic interaction between the carbon-based backbone of the G-PDA-BSA aerogel and the organic solvents can be attributed to the fast adsorption of these non-polar organic solvents.[89] In addition, the hydrophobic regions (from amino acid groups) of denatured BSA may contribute to the removal of these non-polar solvents.[90] Fig. 10(b) presents the regeneration and reuse performance of G-PDA-BSA aerogels for MB removal for different initial concentrations up to 3 cycles. For MB initial concentrations of 25, 100, and 200 mg L^{-1}, the removal efficiencies decreased only slightly after the end of the third cycle; while for the MB concentrations of 50 and 150 mg L^{-1}, the removal efficiency in the third cycle decreased by 80% from the first cycle. Overall, 80–98% of the removal efficiency from the first cycle was retained after the third cycle. Both the results from the recycling of 3D printed G-PDA-BSA aerogels for the removal of organic solvents and MB confirm their potential use as a regenerable adsorbent.

3.4.6 MB removal by the 3D printed aerogel in the flow-through filtration system. A continuous flow-through filtration study was performed to demonstrate the applicability of the fit-for-design 3D printed G-PDA-BSA aerogel as a POU water filtration system. A 3D printed perforated bottle-cap filter system was used to encase and mount the cylindrical G-PDA-BSA aerogel adsorbent with 14 nm diameter and 14 nm height onto a water bottle (Fig. 11a). Fig. 11b and Movie S3 in the ESI† present the filtration process through this 3D printed G-PDA-BSA aerogel-based bottle-cap filtration system. An aqueous solution of MB dye with a concentration of 1 ppm was flowed through the filter under gravitational force and hydrostatic pressure. The average flow rate of the MB dyed water through the filter was measured to be 1.5 mL per minute under a constant hydrostatic pressure of 736 Pa. The MB removal performance of the filter system is expressed as a breakthrough curve in Fig. 11c. More than 85% MB was removed by the filter immediately after the start of the experiment while 100% MB removal efficiency was achieved after passing only 100 mL of water indicating fast adsorption kinetics by the 3D printed aerogel. Furthermore, this 100% MB removal efficiency continued until the filter system reached a breakthrough point after about 4750 mL (*i.e.*, 4.75 L) of permeate flow and the filter system reached the exhaustion point after a flow of ~7000 mL (*i.e.*, 7 L). The MB removal capacity of the G-PDA-BSA aerogel calculated from this flow-through filtration study was 31.66 mg g^{-1} which is close to the batch adsorption capacity of this aerogel for MB *i.e.*, 35.33 mg g^{-1}. Overall, this

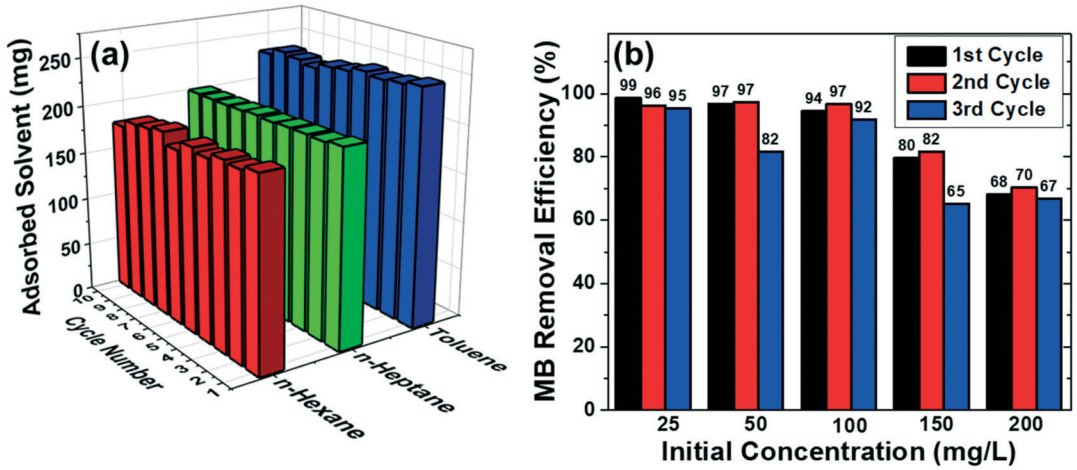

Fig. 10 (a) *n*-Hexane, *n*-heptane and toluene removal performance of the G-PDA-BSA aerogel over 10 repetitive cycles. Initial volume for all the solvents was 300 μL. (b) MB removal performance of the G-PDA-BSA aerogel for 3 repetitive cycles for different initial MB concentrations.

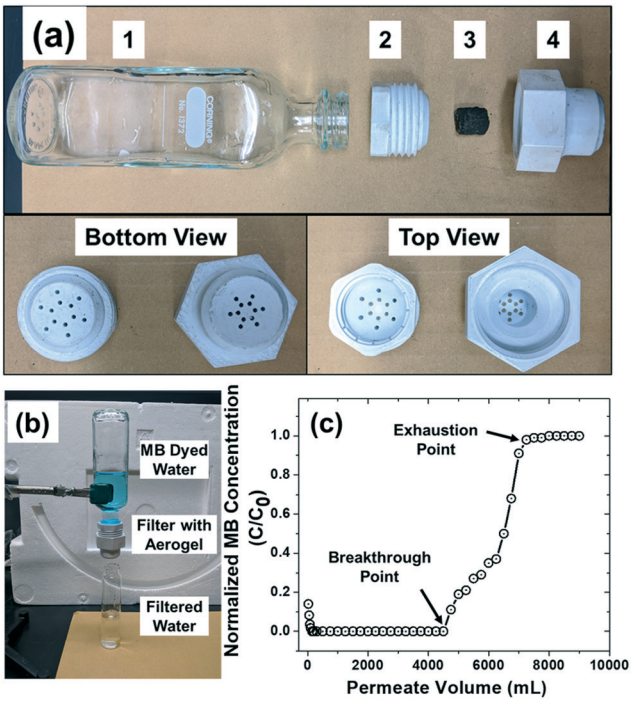

Fig. 11 (a) 3D printed parts of the bottle-cap water filtration system, (b) flow-through experimental setup for the filtration of MB dyed water through the 3D printed G-PDA-BSA aerogel, and (c) breakthrough curve for MB removal by the G-PDA-BSA aerogel during the flow through experiment.

demonstrates the potential ability of our 3D printed G-PDA-BSA aerogel to be employed as a POU filtration system for removing contaminants under flow-through conditions.

4. Conclusion

In this study, a DIW technique was used to 3D print and prepare graphene-biopolymer aerogels for testing their applicability for water treatment. The two biopolymers, PDA and BSA, not only provided appropriate viscoelasticity to the graphene-based ink allowing DIW printability but also dictated the interactions between contaminants and the 3D printed aerogel by changing the surface chemistry and charge. The 3D printed graphene-biopolymer aerogels showed excellent regeneration and reuse potential that is beneficial for their long-term water treatment applications. Furthermore, the flow-through filtration study demonstrated the potential application of 3D printed graphene-biopolymer aerogels in point-of-use filters. The potential and outcomes presented here about the application of 3D printed technology for preparing reusable graphene-based adsorbents can be further extended to other nanomaterials. The flexibility of the 3D printing technology will allow for creation of adsorbents or nano-reactors with different shapes and porous structures that may be used for water treatment needs where shape-effects and hydrodynamics can have an impact on treatment efficiency. This study would further spearhead future research on 3D printed integrated water treatment systems both at the small scale (point-of-use filter systems) and large scale (reactor systems in wastewater treatment plants) by having control over the architecture of both the adsorbent and reactor modules through 3D printing.

Conflicts of interest

The authors declare no conflict of interest.

Acknowledgements

The authors acknowledge the Material Characterization Lab (MCL) at UB for material characterization resources. The authors also acknowledge the Institute of Biotechnology at Cornell University for assistance with nano-CT (instrument grant number NIH S10OD012287) imaging. The authors also acknowledge the support from the National Science Foundation (NSF) through CMMI-1846863 to Dr. Chi Zhou.

The authors also thank Mr. Sarthak Devmurari, a MS graduate from Dr. Zhou's laboratory, for his assistance in the 3D printing process.

References

1 A. Carmalin Sophia, E. C. Lima, N. Allaudeen and S. Rajan, Application of graphene based materials for adsorption of pharmaceutical traces from water and wastewater- a review, *Desalin. Water Treat.*, 2016, **57**(57), 27573–27586.
2 S. Park and R. S. Ruoff, Chemical methods for the production of graphenes, *Nat. Nanotechnol.*, 2009, **4**(4), 217.
3 S. M. Kang, S. Park, D. Kim, S. Y. Park, R. S. Ruoff and H. Lee, Simultaneous Reduction and Surface Functionalization of Graphene Oxide by Mussel-Inspired Chemistry, *Adv. Funct. Mater.*, 2011, **21**(1), 108–112.
4 K. P. Loh, Q. Bao, P. K. Ang and J. Yang, The chemistry of graphene, *J. Mater. Chem.*, 2010, **20**(12), 2277–2289.
5 O. C. Compton, B. Jain, D. A. Dikin, A. Abouimrane, K. Amine and S. T. Nguyen, Chemically active reduced graphene oxide with tunable C/O ratios, *ACS Nano*, 2011, **5**(6), 4380–4391.
6 N. Yousefi, X. Lu, M. Elimelech and N. Tufenkji, Environmental performance of graphene-based 3D macrostructures, *Nat. Nanotechnol.*, 2019, **14**(2), 107–119.
7 J. C. Ruiz-Morales, A. Tarancon, J. Canales-Vazquez, J. Mendez-Ramos, L. Hernandez-Afonso, P. Acosta-Mora, J. R. M. Rueda and R. Fernandez-Gonzalez, Three dimensional printing of components and functional devices for energy and environmental applications, *Energy Environ. Sci.*, 2017, **10**(4), 846–859.
8 Y. Xu, G. Shi and X. Duan, Self-assembled three-dimensional graphene macrostructures: synthesis and applications in supercapacitors, *Acc. Chem. Res.*, 2015, **48**(6), 1666–1675.
9 Y. Xu, K. Sheng, C. Li and G. Shi, Self-assembled graphene hydrogel via a one-step hydrothermal process, *ACS Nano*, 2010, **4**(7), 4324–4330.
10 X. Zhang, Z. Sui, B. Xu, S. Yue, Y. Luo, W. Zhan and B. Liu, Mechanically strong and highly conductive graphene aerogel and its use as electrodes for electrochemical power sources, *J. Mater. Chem.*, 2011, **21**(18), 6494–6497.
11 M. A. Worsley, P. J. Pauzauskie, T. Y. Olson, J. Biener, J. H. Satcher Jr. and T. F. Baumann, Synthesis of graphene aerogel with high electrical conductivity, *J. Am. Chem. Soc.*, 2010, **132**(40), 14067–14069.
12 Z. Chen, W. Ren, L. Gao, B. Liu, S. Pei and H.-M. Cheng, Three-dimensional flexible and conductive interconnected graphene networks grown by chemical vapour deposition, *Nat. Mater.*, 2011, **10**(6), 424.
13 Y. Lin, F. Liu, G. Casano, R. Bhavsar, I. A. Kinloch and B. Derby, Pristine Graphene Aerogels by Room-Temperature Freeze Gelation, *Adv. Mater.*, 2016, **28**(36), 7993–8000.
14 X. Yao and Y. Zhao, Three-dimensional porous graphene networks and hybrids for lithium-ion batteries and supercapacitors, *Chem*, 2017, **2**(2), 171–200.
15 J. A. Lewis, Direct ink writing of 3D functional materials, *Adv. Funct. Mater.*, 2006, **16**(17), 2193–2204.
16 K. Fu, Y. Wang, C. Yan, Y. Yao, Y. Chen, J. Dai, S. Lacey, Y. Wang, J. Wan and T. Li, Graphene Oxide-Based Electrode Inks for 3D-Printed Lithium-Ion Batteries, *Adv. Mater.*, 2016, **28**(13), 2587–2594.
17 L. D. Tijing, J. R. C. Dizon, I. Ibrahim, A. R. N. Nisay, H. K. Shon and R. C. Advincula, 3D printing for membrane separation, desalination and water treatment, *Appl. Mater. Today*, 2020, **18**, 100486.
18 Y. Dong, S.-Q. Fan, Y. Shen, J.-X. Yang, P. Yan, Y.-P. Chen, J. Li, J.-S. Guo, X.-M. Duan and F. Fang, A novel bio-carrier fabricated using 3D printing technique for wastewater treatment, *Sci. Rep.*, 2015, **5**, 12400.
19 E. Mousset, V. H. Weiqi, B. F. Y. Kai, J. S. Koh, J. W. Tng, Z. Wang and O. Lefebvre, A new 3D-printed photoelectrocatalytic reactor combining the benefits of a transparent electrode and the Fenton reaction for advanced wastewater treatment, *J. Mater. Chem. A*, 2017, **5**(47), 24951–24964.
20 Z. Wang, J. Wang, M. Li, K. Sun and C.-J. Liu, Three-dimensional printed acrylonitrile butadiene styrene framework coated with Cu-BTC metal-organic frameworks for the removal of methylene blue, *Sci. Rep.*, 2014, **4**, 5939.
21 P. He, X. Tang, L. Chen, P. Xie, L. He, H. Zhou, D. Zhang and T. Fan, Patterned Carbon Nitride–Based Hybrid Aerogel Membranes via 3D Printing for Broadband Solar Wastewater Remediation, *Adv. Funct. Mater.*, 2018, 1801121.
22 C. Zhu, T. Liu, F. Qian, T. Y.-J. Han, E. B. Duoss, J. D. Kuntz, C. M. Spadaccini, M. A. Worsley and Y. Li, Supercapacitors Based on Three-Dimensional Hierarchical Graphene Aerogels with Periodic Macropores, *Nano Lett.*, 2016, **16**(6), 3448–3456.
23 X. Tang, H. Zhou, Z. Cai, D. Cheng, P. He, P. Xie, D. Zhang and T. Fan, Generalized 3D Printing of Graphene-Based Mixed-Dimensional Hybrid Aerogels, *ACS Nano*, 2018, **12**(4), 3502–3511.
24 Y. Jiang, Z. Xu, T. Huang, Y. Liu, F. Guo, J. Xi, W. Gao and C. Gao, Direct 3D printing of ultralight graphene oxide aerogel microlattices, *Adv. Funct. Mater.*, 2018, **28**(16), 1707024.
25 A. E. Jakus, E. B. Secor, A. L. Rutz, S. W. Jordan, M. C. Hersam and R. N. Shah, Three-dimensional printing of high-content graphene scaffolds for electronic and biomedical applications, *ACS Nano*, 2015, **9**(4), 4636–4648.
26 Y. Yao, K. K. Fu, C. Yan, J. Dai, Y. Chen, Y. Wang, B. Zhang, E. Hitz and L. Hu, Three-dimensional printable high-temperature and high-rate heaters, *ACS Nano*, 2016, **10**(5), 5272–5279.
27 Y. Yang, Y. S. Ok, K.-H. Kim, E. E. Kwon and Y. F. Tsang, Occurrences and removal of pharmaceuticals and personal care products (PPCPs) in drinking water and water/sewage treatment plants: A review, *Sci. Total Environ.*, 2017, **596**, 303–320.
28 N. Farnad, K. Farhadi and N. H. Voelcker, Polydopamine nanoparticles as a new and highly selective biosorbent for the removal of copper (II) ions from aqueous solutions, *Water, Air, Soil Pollut.*, 2012, **223**(6), 3535–3544.

29 J. Deng, B. Lei, A. He, X. Zhang, L. Ma, S. Li and C. Zhao, Toward 3D graphene oxide gels based adsorbents for high-efficient water treatment via the promotion of biopolymers, *J. Hazard. Mater.*, 2013, **263**, 467–478.
30 J. Fu, Z. Chen, M. Wang, S. Liu, J. Zhang, J. Zhang, R. Han and Q. Xu, Adsorption of methylene blue by a high-efficiency adsorbent (polydopamine microspheres): kinetics, isotherm, thermodynamics and mechanism analysis, *Chem. Eng. J.*, 2015, **259**, 53–61.
31 E. Papastavros, R. A. Remmers, D. D. Snow, D. A. Cassada and D. S. Hage, Affinity extraction of emerging contaminants from water based on bovine serum albumin as a binding agent, *J. Sep. Sci.*, 2018, **41**(5), 1074–1082.
32 Y. Wang, S. Wang, H. Niu, Y. Ma, T. Zeng, Y. Cai and Z. Meng, Preparation of polydopamine coated Fe3O4 nanoparticles and their application for enrichment of polycyclic aromatic hydrocarbons from environmental water samples, *J. Chromatogr. A*, 2013, **1283**, 20–26.
33 F. Guo, M. Creighton, Y. Chen, R. Hurt and I. Külaots, Porous structures in stacked, crumpled and pillared graphene-based 3D materials, *Carbon*, 2014, **66**, 476–484.
34 A. Masud, Y. Cui, J. D. Atkinson and N. Aich, Shape matters: Cr (VI) removal using iron nanoparticle impregnated 1-D vs 2-D carbon nanohybrids prepared by ultrasonic spray pyrolysis, *J. Nanopart. Res.*, 2018, **20**(3), 64.
35 S. Mallakpour, A. Abdolmaleki and S. Borandeh, Surface functionalization of GO, preparation and characterization of PVA/TRIS-GO nanocomposites, *Polymer*, 2015, **81**, 140–150.
36 Y. Deng, Y. Li, J. Dai, M. Lang and X. Huang, Functionalization of graphene oxide towards thermo-sensitive nanocomposites via moderate in situ SET-LRP, *J. Polym. Sci., Part A: Polym. Chem.*, 2011, **49**(22), 4747–4755.
37 H. Gao, Y. Sun, J. Zhou, R. Xu and H. Duan, Mussel-Inspired Synthesis of Polydopamine-Functionalized Graphene Hydrogel as Reusable Adsorbents for Water Purification, *ACS Appl. Mater. Interfaces*, 2013, **5**(2), 425–432.
38 L. Q. Xu, W. J. Yang, K.-G. Neoh, E.-T. Kang and G. D. Fu, Dopamine-induced reduction and functionalization of graphene oxide nanosheets, *Macromolecules*, 2010, **43**(20), 8336–8339.
39 C. Cheng, S. Nie, S. Li, H. Peng, H. Yang, L. Ma, S. Sun and C. Zhao, Biopolymer functionalized reduced graphene oxide with enhanced biocompatibility via mussel inspired coatings/anchors, *J. Mater. Chem. B*, 2013, **1**(3), 265–275.
40 J. I. Boye, I. Alli and A. A. Ismail, Interactions involved in the gelation of bovine serum albumin, *J. Agric. Food Chem.*, 1996, **44**(4), 996–1004.
41 M. E. Hines and E. A. Foegeding, Interactions of alpha-lactalbumin and bovine serum albumin with beta-lactoglobulin in thermally induced gelation, *J. Agric. Food Chem.*, 1993, **41**(3), 341–346.
42 M. Murata, F. Tani, T. Higasa, N. Kitabatake and E. Doi, Heat-induced transparent gel formation of bovine serum albumin, *Biosci., Biotechnol., Biochem.*, 1993, **57**(1), 43–46.
43 A. M'barki, L. Bocquet and A. Stevenson, Linking rheology and printability for dense and strong ceramics by direct ink writing, *Sci. Rep.*, 2017, **7**(1), 1–10.
44 J. Miao, H. Liu, W. Li and X. Zhang, Mussel-Inspired Polydopamine-Functionalized Graphene as a Conductive Adhesion Promoter and Protective Layer for Silver Nanowire Transparent Electrodes, *Langmuir*, 2016, **32**(21), 5365–5372.
45 Y. Luo, S. Jiang, Q. Xiao, C. Chen and B. Li, Highly reusable and superhydrophobic spongy graphene aerogels for efficient oil/water separation, *Sci. Rep.*, 2017, **7**(1), 1–10.
46 B. D. Ossonon and D. Bélanger, Synthesis and characterization of sulfophenyl-functionalized reduced graphene oxide sheets, *RSC Adv.*, 2017, **7**(44), 27224–27234.
47 A. Alazmi, O. El Tall, S. Rasul, M. N. Hedhili, S. P. Patole and P. M. Costa, A process to enhance the specific surface area and capacitance of hydrothermally reduced graphene oxide, *Nanoscale*, 2016, **8**(41), 17782–17787.
48 M. Toupin and D. Bélanger, Spontaneous Functionalization of Carbon Black by Reaction with 4-Nitrophenyldiazonium Cations, *Langmuir*, 2008, **24**(5), 1910–1917.
49 A. Le Comte, D. Chhin, A. Gagnon, R. Retoux, T. Brousse and D. Bélanger, Spontaneous grafting of 9, 10-phenanthrenequinone on porous carbon as an active electrode material in an electrochemical capacitor in an alkaline electrolyte, *J. Mater. Chem. A*, 2015, **3**(11), 6146–6156.
50 I.-M. Tang, N. Krishnamra, N. Charoenphandhu, R. Hoonsawat and W. Pon-On, Biomagnetic of apatite-coated cobalt ferrite: a core–shell particle for protein adsorption and pH-controlled release, *Nanoscale Res. Lett.*, 2011, **6**(1), 19.
51 L. Feng, G. Gao, P. Huang, X. Wang, C. Zhang, J. Zhang, S. Guo and D. Cui, Preparation of Pt Ag alloy nanoisland/graphene hybrid composites and its high stability and catalytic activity in methanol electro-oxidation, *Nanoscale Res. Lett.*, 2011, **6**(1), 551.
52 J. Liu, S. Fu, B. Yuan, Y. Li and Z. Deng, Toward a universal "adhesive nanosheet" for the assembly of multiple nanoparticles based on a protein-induced reduction/decoration of graphene oxide, *J. Am. Chem. Soc.*, 2010, **132**(21), 7279–7281.
53 I. K. Moon, J. Lee, R. S. Ruoff and H. Lee, Reduced graphene oxide by chemical graphitization, *Nat. Commun.*, 2010, **1**, 73.
54 L. Li, W. Feng and P. Ji, Protein adsorption on functionalized multiwalled carbon nanotubes with amino-cyclodextrin, *AIChE J.*, 2011, **57**(12), 3507–3513.
55 J. Luo, N. Zhang, R. Liu and X. Liu, In situ green synthesis of Au nanoparticles onto polydopamine-functionalized graphene for catalytic reduction of nitrophenol, *RSC Adv.*, 2014, **4**(110), 64816–64824.
56 F. Wang, R. Han, G. Liu, H. Chen, T. Ren, H. Yang and Y. Wen, Construction of polydopamine/silver nanoparticles multilayer film for hydrogen peroxide detection, *J. Electroanal. Chem.*, 2013, **706**, 102–107.
57 M. J. McAllister, J.-L. Li, D. H. Adamson, H. C. Schniepp, A. A. Abdala, J. Liu, M. Herrera-Alonso, D. L. Milius, R. Car and R. K. Prud'homme, Single sheet functionalized graphene by oxidation and thermal expansion of graphite, *Chem. Mater.*, 2007, **19**(18), 4396–4404.

58 R. N. Grass and W. J. Stark, Flame synthesis of calcium-, strontium-, barium fluoride nanoparticles and sodium chloride, *Chem. Commun.*, 2005, 1767–1769.
59 E. Askari and S. M. Naghib, A Novel Approach to Facile Synthesis and Biosensing of the Protein-Regulated Graphene, *Int. J. Electrochem. Sci.*, 2018, **13**, 886–897.
60 S. Kellici, J. Acord, J. Ball, H. S. Reehal, D. Morgan and B. Saha, A single rapid route for the synthesis of reduced graphene oxide with antibacterial activities, *RSC Adv.*, 2014, **4**(29), 14858–14861.
61 K. Griebenow and A. M. Klibanov, On protein denaturation in aqueous– organic mixtures but not in pure organic solvents, *J. Am. Chem. Soc.*, 1996, **118**(47), 11695–11700.
62 R. I. Litvinov, D. A. Faizullin, Y. F. Zuev and J. W. Weisel, The α-helix to β-sheet transition in stretched and compressed hydrated fibrin clots, *Biophys. J.*, 2012, **103**(5), 1020–1027.
63 Y. Mi, Z. Wang, X. Liu, S. Yang, H. Wang, J. Ou, Z. Li and J. Wang, A simple and feasible in-situ reduction route for preparation of graphene lubricant films applied to a variety of substrates, *J. Mater. Chem.*, 2012, **22**(16), 8036–8042.
64 A. H. Clark, D. H. P. Saunderson and A. Suggett, Infrared and laser-raman spectroscopic studies of thermally-induced globular protein gels, *Int. J. Pept. Protein Res.*, 1981, **17**(3), 353–364.
65 Y. Zhang, H.-L. Ma, Q. Zhang, J. Peng, J. Li, M. Zhai and Z.-Z. Yu, Facile synthesis of well-dispersed graphene by γ-ray induced reduction of graphene oxide, *J. Mater. Chem.*, 2012, **22**(26), 13064–13069.
66 Y. Liao, M. Wang and D. Chen, Preparation of polydopamine-modified graphene oxide/chitosan aerogel for uranium (VI) adsorption, *Ind. Eng. Chem. Res.*, 2018, **57**(25), 8472–8483.
67 H. Luo, C. Gu, W. Zheng, F. Dai, X. Wang and Z. Zheng, Facile synthesis of novel size-controlled antibacterial hybrid spheres using silver nanoparticles loaded with polydopamine spheres, *RSC Adv.*, 2015, **5**(18), 13470–13477.
68 A. Gebregeorgis, C. Bhan, O. Wilson and D. Raghavan, Characterization of Silver/Bovine Serum Albumin (Ag/BSA) nanoparticles structure: Morphological, compositional, and interaction studies, *J. Colloid Interface Sci.*, 2013, **389**(1), 31–41.
69 V. A. Borzova, K. A. Markossian, N. A. Chebotareva, S. Y. Kleymenov, N. B. Poliansky, K. O. Muranov, V. A. Stein-Margolina, V. V. Shubin, D. I. Markov and B. I. Kurganov, Kinetics of thermal denaturation and aggregation of bovine serum albumin, *PLoS One*, 2016, **11**(4), e0153495.
70 R. Yu, Y. Shi, D. Yang, Y. Liu, J. Qu and Z.-Z. Yu, Graphene oxide/chitosan aerogel microspheres with honeycomb-cobweb and radially oriented microchannel structures for broad-spectrum and rapid adsorption of water contaminants, *ACS Appl. Mater. Interfaces*, 2017, **9**(26), 21809–21819.
71 G. Aylaz, M. Okan, M. Duman and H. M. Aydin, Study on Cost-Efficient Carbon Aerogel to Remove Antibiotics from Water Resources, *ACS Omega*, 2020, **5**(27), 16635–16644.
72 C.-H. Weng, Modeling Pb(II) adsorption onto sandy loam soil, *J. Colloid Interface Sci.*, 2004, **272**(2), 262–270.
73 M. Szabó, J. Kalmár, T. Ditrói, G. Bellér, G. Lente, N. Simic and I. Fábián, Equilibria and kinetics of chromium(VI) speciation in aqueous solution – A comprehensive study from pH 2 to 11, *Inorg. Chim. Acta*, 2018, **472**, 295–301.
74 L. Shao, R. Zhang, J. Lu, C. Zhao, X. Deng and Y. Wu, Mesoporous silica coated polydopamine functionalized reduced graphene oxide for synergistic targeted chemo-photothermal therapy, *ACS Appl. Mater. Interfaces*, 2017, **9**(2), 1226–1236.
75 T.-Y. Lin and D.-H. Chen, One-step green synthesis of arginine-capped iron oxide/reduced graphene oxide nanocomposite and its use for acid dye removal, *RSC Adv.*, 2014, **4**(56), 29357–29364.
76 J. Xu, A. Ma, T. Liu, C. Lu, D. Wang and H. Xu, Janus-like Pickering emulsions and their controllable coalescence, *Chem. Commun.*, 2013, **49**(92), 10871–10873.
77 Z.-H. Huang, X. Zheng, W. Lv, M. Wang, Q.-H. Yang and F. Kang, Adsorption of lead (II) ions from aqueous solution on low-temperature exfoliated graphene nanosheets, *Langmuir*, 2011, **27**(12), 7558–7562.
78 Q. Zhang, Q. Yang, P. Phanlavong, Y. Li, Z. Wang, T. Jiao and Q. Peng, Highly efficient lead (II) sequestration using size-controllable polydopamine microspheres with superior application capability and rapid capture, *ACS Sustainable Chem. Eng.*, 2017, **5**(5), 4161–4170.
79 B. Saha, S. Chakraborty and G. Das, A Rational Approach for Controlled Adsorption of Metal Ions on Bovine Serum Albumin– Malachite Bionanocomposite, *J. Phys. Chem. C*, 2010, **114**(21), 9817–9825.
80 H. Yan, X. Tao, Z. Yang, K. Li, H. Yang, A. Li and R. Cheng, Effects of the oxidation degree of graphene oxide on the adsorption of methylene blue, *J. Hazard. Mater.*, 2014, **268**, 191–198.
81 I. J. Buerge and S. J. Hug, Kinetics and pH dependence of chromium (VI) reduction by iron (II), *Environ. Sci. Technol.*, 1997, **31**(5), 1426–1432.
82 Y. Zhang, Z. Qi, D. Zheng, C. Li and Y. Liu, Interactions of Chromium (III) and Chromium (VI) with Bovine Serum Albumin Studied by UV Spectroscopy, Circular Dichroism, and Fluorimetry, *Biol. Trace Elem. Res.*, 2009, **130**(2), 172–184.
83 Y. Hedberg, M. Lundin, J. Jacksén, Å. Emmer, E. Blomberg and I. Odnevall Wallinder, Chromium–protein complexation studies by adsorptive cathodic stripping voltammetry and MALDI-TOF–MS, *J. Appl. Electrochem.*, 2012, **42**(5), 349–358.
84 L. Yao, X. Xue, P. Yu, Y. Ni and F. Chen, Evans blue dye: a revisit of its applications in biomedicine, *Contrast Media Mol. Imaging*, 2018, **2018**, 7628037.
85 Y. Ying, P. He, G. Ding and X. Peng, Ultrafast adsorption and selective desorption of aqueous aromatic dyes by graphene sheets modified by graphene quantum dots, *Nanotechnology*, 2016, **27**(24), 245703.

86 US Research Nanomaterials, Inc., https://www.us-nano.com/inc/sdetail/25856 (accessed September 03, 2020).
87 Sigma-Aldrich, https://www.sigmaaldrich.com/catalog/product/sigma/h8502?lang=en&region=US (accessed September 03).
88 Sigma-Aldrich, https://www.sigmaaldrich.com/catalog/product/sigma/a9418?lang=en&region=US (accessed September 03).
89 S. Pourmand, M. Abdouss and A. Rashidi, Fabrication of nanoporous graphene by chemical vapor deposition (CVD) and its application in oil spill removal as a recyclable nanosorbent, *J. Ind. Eng. Chem.*, 2015, **22**, 8–18.
90 K. Yasuda, R. Nakamura and S. Hayakawa, Factors Affecting Heat-Induced Gel Formation of Bovine Serum Albumin, *J. Food Sci.*, 1986, **51**(5), 1289–1292.

